CHEMISTRY OF MATERIALS

Open Access

pubs.acs.org/cm

Article

Length-Scale-Dependent Ion Dynamics in Ca-Doped Na_3PS_4

Katharina Hogrefe,* Jana Königsreiter, Anna Bernroitner, Bernhard Gadermaier, Sharon E. Ashbrook, and H. Martin R. Wilkening*

Cite This: https://doi.org/10.1021/acs.chemmater.3c02874

Read Online

ACCESS | Metrics & More | Article Recommendations | Supporting Information

ABSTRACT: The sodium ion conductor Na_3PS_4 is a promising electrolyte for future all-solid-state batteries using Na^+ ions as ionic charge carriers. Its readily available components make it a compelling and more sustainable alternative to recent Li-ion technologies. At ambient temperature, the ionic conductivity is in the order of 10^{-4} S cm^{-1}, which can be optimized by adjusting doping and processing parameters. Even though several studies have focused on explaining the dynamic properties of doped and undoped Na_3PS_4, the driving forces that lead to fast Na^+ exchange are not yet completely understood. Here, we synthesized nanocrystalline, defect-rich cubic Na_3PS_4 via a solid-state synthesis route and compared its properties with those of highly crystalline Ca-doped $Na_{3-2x}Ca_xPS_4$. The interconnected effects of doping and synthesis procedure on both structure and dynamic properties are investigated. X-ray diffraction reveals that the undoped samples show clear cubic and tetragonal symmetry, while for the doped samples, a phase mixture of both polymorphs is seen. High-resolution ^{23}Na magic angle spinning NMR spectra acquired at temperatures as low as −60 °C clearly reveal two different Na sites when ionic motion is partially frozen out. Ion dynamics of the powder samples were analyzed using high-precision broadband impedance spectroscopy and variable-temperature, time-domain ^{23}Na NMR spin−lattice relaxation rate measurements. Localized Na^+ jumps detected by NMR showed higher energy barriers but faster Na^+ dynamics for the Ca-doped samples. A similar trend was observed in conductivity spectroscopy with lowest activation energy for Na-ion transport in tetragonal Na_3PS_4 but highest attempt frequencies for the hopping motion in Ca-doped Na_3PS_4 with x = 0.135, making the doped sample the superior ion conductor at *elevated* temperatures. Our study highlights the importance of breaking down ionic transport in its elemental steps to understand the complex interplay of intrinsic and extrinsic parameters in solid electrolyte materials.

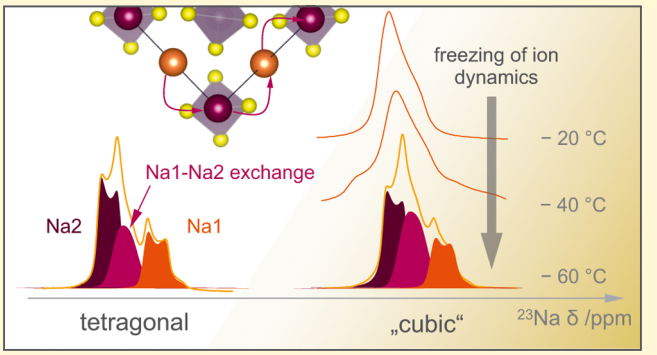

KEYWORDS: *ion, conductor, Na_3PS_4, solid electrolyte, Na_+ conductor, ionic conductor, ionic conductivity, doping, dynamic properties, ^{23}Na NMR, MAS NMR, ionic motion, ion dynamics, spectroscopy, impedance spectroscopy*

1. INTRODUCTION

The largest global crisis, which is caused by the immense increase of anthropogenic greenhouse gases, forces us to radically change our energy management from an economy that is based on fossil fuels to a sustainable circular system mainly using renewable resources.[1] To achieve this goal, we need to invent new and to drastically improve existing technologies to convert and to store energy in a sustainable manner.[1−4] Electrochemical energy storage plays a key role in this research field because of the high degree of effectiveness of, e.g., batteries that use small and fast ions acting as ionic charge carriers.[1,5]

At present, lithium-ion batteries dominate the market for both small consumer devices, such as mobile phones and notebooks, and electric vehicles.[6] The availability of lithium[7,8] is, however, expected to become a critical issue because of the rising demand from the expanding electric vehicle industry in combination with geopolitical conflicts. In terms of important sustainable aspects, sodium is the best alternative to lithium considering the high natural abundance of Na in both the Earth's crust and in seawater.[9] As a result, the price of many sodium-bearing raw compounds is considerably lower than that of raw materials containing lithium. Converting a lithium-based battery into a sodium one is, however, fraught with difficulties because of the different chemical and electrochemical properties of the sodium compounds.[10−12] Their higher weight and their lower electrochemical potentials lead to an overall decrease in capacity as compared to systems relying on Li^+. Even though sodium-ion battery technology is again on the rise, the type of application it will enter is not yet completely settled. Its electrochemical

Received: November 10, 2023
Revised: December 14, 2023
Accepted: December 15, 2023

properties[10] would preferentially suggest its use in stationary applications, e.g., in energy grids that need electrochemical storage devices to mitigate intermittency issues when electricity is converted from wind or solar power into electrochemical energy.[1,5]

Besides Na-ion batteries with liquid electrolytes,[9,10,13] we have witnessed an increasing demand for solid or even ceramic Na-ion conductors[14−16] as they might pave the way toward safe, nonflammable all-solid-state Na-battery systems.[15−18] Only few groups of solid electrolytes have been considered so far for the use in Na-ion batteries, such as β''-alumina,[19] NASICON-type (Na superionic conductor) materials,[20−26] and the sodium variants of the well-known Li^+ conductor LGPS ($Li_{10}GeP_2S_{12}$), which are based on $Na_{11}Sn_2PS_{12}$.[27] In particular, among these promising ionic conductors, we also find Na_3PS_4, first reported in 1992 to have an ionic conductivity of approximately 4.2×10^{-6} S cm^{-1} at ambient temperature.[28] This thiophosphate occurs in three different structural modifications, one of them, γ-Na_3PS_4, is only stable above 490 °C.[29] The other two forms, cubic and tetragonal Na_3PS_4, show relatively high ionic conductivities at room temperature.[30,31] Originally, it has been reported that the ionic conductivity of the cubic polymorph clearly exceeds that of the tetragonal form. As an example, Hayashi et al.[30] managed to stabilize cubic Na_3PS_4 at room temperature via a synthesis route employing high-energy ball milling; subsequent annealing of the ball-milled mixture yielded a compound with ionic conductivities in the range of 10^{-4} S cm^{-1} (20 °C). There is, however, an ongoing debate on the question whether the cubic symmetry is indeed responsible for the higher conductivity compared to the tetragonal form of Na_3PS_4.[31,32]

This important relation between local and overall crystal structure on the one hand and the dynamic properties of Na_3PS_4 on the other has been widely discussed over the last couple of years. In 2018, Takeuchi et al.[31] investigated the influence of different synthesis routes on ionic conductivity while keeping the stoichiometry of the samples untouched. They found a tetragonal phase with a larger lattice volume to have the highest conductivity, which was characterized by the occupation of interstitial Na sites. They also compared different tetragonal phases to a seemingly cubic phase, which showed lower-conductivity values σ' at ambient temperature as compared to the superior tetragonal phase. The authors reported very broad X-ray reflections for the cubic phase. A reinvestigation of the crystal symmetry by Rietveld analysis showed, however, that the data obtained could also be interpreted by a tetragonal lattice with no vacancies on the Na sites. Takeuchi et al. concluded that the overall "cubic" phase is in fact formed of microdomains crystallizing with tetragonal symmetry, finally resulting in the observation of a pseudocubic characteristic as a result of X-ray diffraction (XRD) probing average lattice properties.[31] A similar conclusion has been presented by Krauskopf et al.[32] Despite appearing cubic on the average scale by Bragg diffraction measurements, pair distribution function analysis showed that also local structures adopt tetragonal symmetry. The authors concluded that ionic conductivity in Na_3PS_4 is not governed by the underlying crystal structure but by defect concentrations and crystal size effects.[32] We believe that a consistent and final picture regarding these competing effects on the ionic transport properties is, however, still missing for Na_3PS_4.

Next to optimizing the synthesis conditions, several groups tested different doping strategies to enhance the ionic conductivity of Na_3PS_4.[33,34] Partly exchanging the S^{2-} anions by halide ions leads to a lower overall negative charge within the structure. To compensate for this charge imbalance, negatively charged Na vacancies, $V^{\bullet}_{Na}$, are generated. Modeling approaches show low dopant formation energies for the halides F^-, Cl^-, Br^-, and I^-.[35] Substitution of P^{5+} by Si^{4+} also resulted in increased ionic conductivity by a similar vacancy generation mechanism.[34] A different approach is to directly substitute the mobile Na^+ ions by another ion of higher positive charge to again generate sodium vacancies. The ionic radius of Ca^{2+} is similar to Na^+ and, therefore, highly suitable for this approach.

Ca^{2+} doping of Na_3PS_4 was first evaluated by Moon et al.[33] in an experimental study that was complemented by density functional theory (DFT) calculations. The authors showed that Ca^{2+} doping causes an increase in ionic conductivity, with the compound $Na_{2.73}Ca_{0.135}PS_4$ exhibiting the highest value $\sigma' \approx 1$ mS cm^{-1} under ambient conditions. Importantly, if analyzed in the frame of an Arrhenius diagram, the Arrhenius lines of σ' of the Ca-doped samples are characterized by a higher prefactor and a higher activation energy compared to those of the undoped samples. Interestingly, the authors observed a tetragonal-to-cubic phase transformation upon Ca^{2+} incorporation. Their DFT calculations suggest facilitated migration in the vacancy-rich Ca-doped phases as compared to the vacancy-free structure. Ca^{2+} doping results, however, in higher energy barriers because of vacancy trapping close to the Ca^{2+} ions. Nonetheless, the doped samples are characterized by a large number fraction of vacancies $V_{Na}^{\bullet}$ on the Na sites, enhancing the Arrhenius prefactor of the ionic conductivity and outweighing the unfavorable increase in activation energy. Using image-nudged elastic band methods, Huang et al.[36] also found faster Na^+ migration in Ca-doped Na_3PS_4. Their simulated results do, however, show lower migration barriers in the Ca-bearing samples conflicting the experimental data. This discrepancy is still not sufficiently discussed, blurring the overall picture of ion transport in undoped and Ca-doped Na_3PS_4.

Here, we tested and elucidated the effect of different Ca^{2+} substitution levels and processing conditions in a series of Ca-bearing Na_3PS_4 samples and their influence on both macroscopic and microscopic dynamic properties. We prepared our samples via solid-state synthesis routes using high-energy ball milling and subsequent annealing steps. To verify their purity, local and long-range (averaged) structures were characterized by powder XRD and magic angle spinning (MAS), respectively. In particular, ^{23}Na MAS NMR carried out at low temperatures helped directly prove the local geometry of the Na ions in tetragonal and nominal cubic Na_3PS_4. Data from conductivity spectroscopy were used to study ionic transport in both the bulk areas and across grain boundary regions. We were able to show the dual effect of doping on macroscopic diffusion and propose that the synthesis route is of a similar importance as the dopant level. In addition, we investigated dynamic properties of the samples directly by static ^{23}Na NMR spin−lattice relaxation (SLR) measurements[37,38] which are helpful to elucidate diffusion processes at the atomic length scale. The trend of the activation energies obtained in this way from ^{23}Na NMR agrees well with data from conductivity spectroscopy; however, the ^{23}Na NMR SLR rate maxima appear at low temperature and point to enhanced Na^+ diffusion in the Ca-doped samples at short time scales. Our results show the complex interplay of doping strategies and synthesis conditions and underline the importance of studying ionic diffusion over a broad dynamic window to understand ion transport in these highly relevant solid electrolytes for new energy storage devices.

https://doi.org/10.1021/acs.chemmater.3c02874
Chem. Mater. XXXX, XXX, XXX−XXX

2. RESULTS AND DISCUSSION

2.1. Structural Investigation by XRD and NMR. The crystal structure of Na_3PS_4 is depicted in Figure 1. Both the cubic and the tetragonal phases[28] show high symmetry, differing in an elongation of the *c*-axis by 1.8% for the tetragonal phase, thereby creating two crystallographic Na sites in this form. X-ray powder diffraction was used to characterize the structure and to prove successful doping; the corresponding patterns are shown in Figure 2a. Besides Ca-free tetragonal and cubic Na_3PS_4, two samples with different dopant levels of $Na_{3-2x}Ca_xPS_4$, viz. x = 0.0675 and x = 0.135, were prepared.

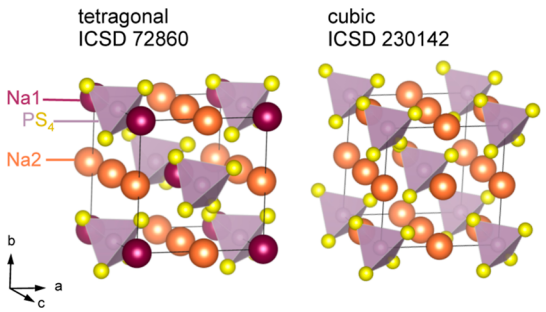

Figure 1. Crystal structures of tetragonal and cubic Na_3PS_4. PS_4^{3-} units are shown as purple tetrahedra with sulfur (yellow spheres) located on the corners. Sodium ions, Na^+, located on the two crystallographic inequivalent positions in tetragonal Na_3PS_4 are represented by orange and purple spheres, respectively. In cubic Na_3PS_4, only a single Na site is seen.

For the sample prepared in a similar way to the doped ones but without the addition of Ca, we see a good correlation with the tetragonal reference pattern. Also, for the sample having a low Ca content (x = 0.0675), we observe a splitting of the reflections pointing to a symmetry lower than cubic. In contrast, the pattern of the sample with a high Ca content (x = 0.135) resembles that of the cubic reference rather than that of tetragonal Na_3PS_4. However, some of the reflections are asymmetric in shape also for this sample; see the reflections at 31° and 36° 2θ. Accordingly, this higher Ca-doped sample is clearly not purely cubic but also shows some tetragonal characteristics. The same holds for the lower doped sample with x = 0.0675, which predominantly appears as tetragonal but deviating peak shapes from the tetragonal reference indicate, from an average point of view, also the presence of cubic features. We conclude that there might be a gradual transition of the samples to appear dominantly with tetragonal or cubic symmetry on average. Regarding the symmetry, the cubic sample is slightly more symmetric than the tetragonal one. The latter shows an elongated *c*-axis leading to a splitting of different reflections. The terms "cubic" and "tetragonal" refer to perfect symmetry with regard to the, respective, reference crystal structures. We have to consider that a perfectly cubic symmetry is unlikely to be observed in a powder sample, even more so in a ball-milled sample annealed at quite low temperatures. The term "cubic" will here be used to describe the average crystal symmetry as seen by powder XRD. As will be discussed later on, also for seemingly cubic long-range symmetry, NMR will reveal local tetragonal structures.

Regarding the transition from a tetragonal to a more cubic-like symmetry, a similar behavior has been observed by Moon et al.,[33] reporting that Ca doping stabilizes the cubic phase. For a sample with a Ca content of x = 0.135, they found a phase fraction of 91.7% for the cubic phase, which agrees with our data. However, for a lower dopant level, we find a predominantly tetragonal characteristic contrasting prior experimental work.[33] In the present case, however, Rietveld refinements did not give reliable results due to the very similar symmetry of tetragonal and cubic Na_3PS_4 and the resulting overlap of all reflections. Especially, if lattice parameters and phase fractions are refined at the same time, new uncertainties are added to the refinement.

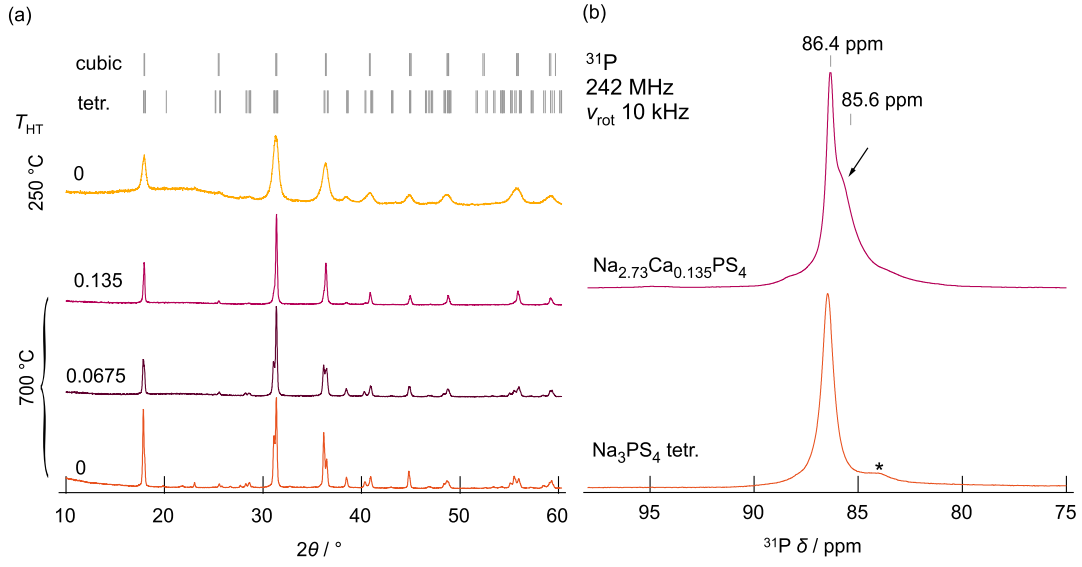

Figure 2. (a) X-ray powder diffractograms of Ca-doped $Na_{3-2x}Ca_xPS_4$ (x = 0.0675 and x = 0.135). The patterns of Ca-free Na_3PS_4 with tetragonal (orange) and cubic (yellow) symmetry are also shown. The reference pattern were taken from the Inorganic Crystal Structure Database (ICSD). For comparison, the number and the position of the reference reflections of the cubic and the tetragonal phase are included as small bars at the top of the graph. Temperatures of the, respective, heat treatment procedures, T_{HT}, are shown on the left-hand side. (b) ^{31}P MAS NMR spectra of $Na_{2.73}Ca_{0.135}PS_4$ and Na_3PS_4 crystallizing with tetragonal symmetry. A shoulder appears at a chemical shift value 85.6 ppm for the doped sample. A minor impurity in Na_3PS_4 is marked by an asterisk. Chemical shifts are referenced with respect to H_3PO_4.

https://doi.org/10.1021/acs.chemmater.3c02874
Chem. Mater. XXXX, XXX, XXX−XXX

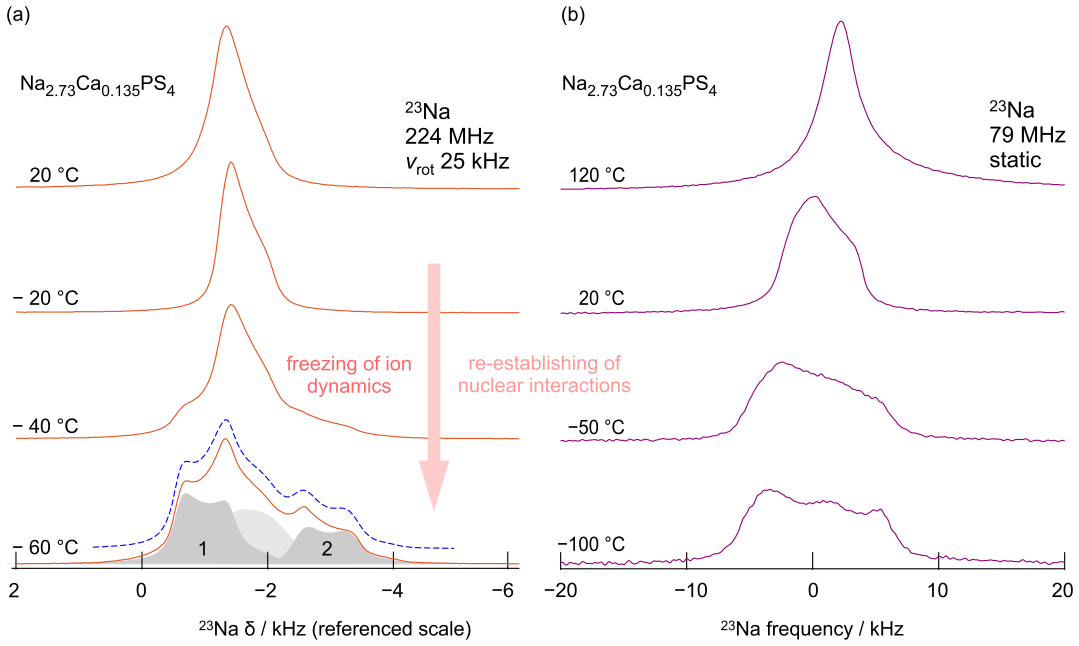

Figure 3. (a) ^{23}Na MAS spectra of $Na_{2.73}Ca_{0.135}PS_4$ acquired at a spinning speed of 25 kHz and recorded at the nominal temperatures indicated. The line recorded at −60 °C is deconvoluted such that two lines affected by quadrupolar interactions are obtained that represent the sites Na1 and Na2. The Gaussian-shaped line in between these lines is due to exchange processes leading to the beginning of a coalesced signal. (b) ^{23}Na NMR lines of the same sample but recorded under static, i.e., non-MAS, conditions at temperatures ranging from −100 to 120 °C.

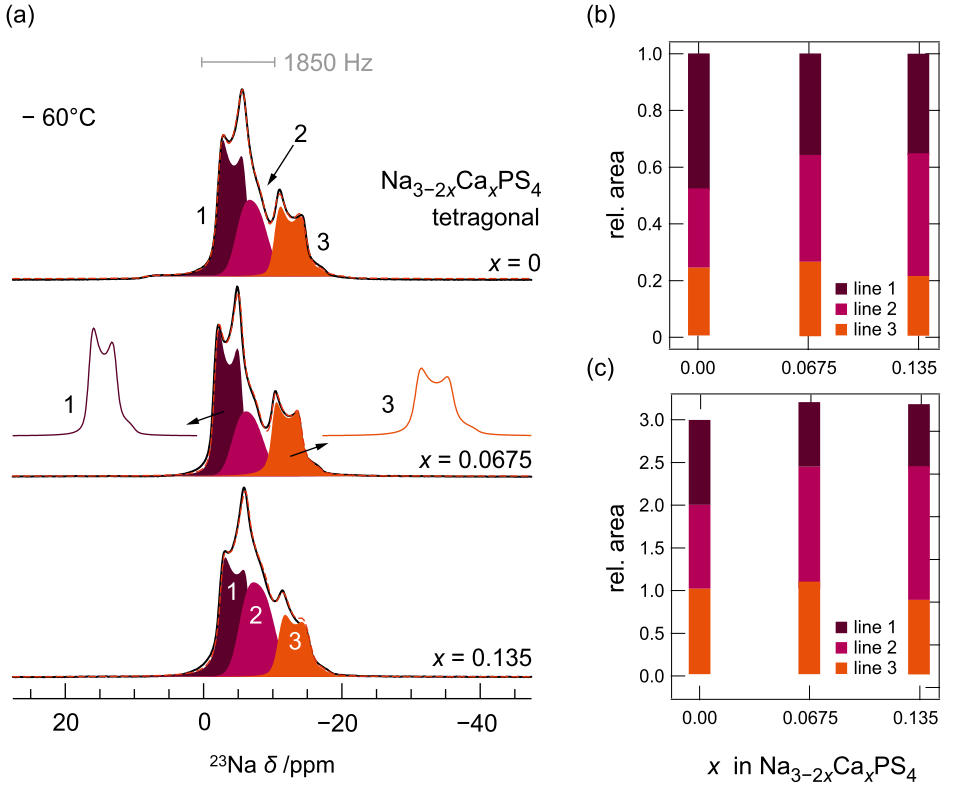

Figure 4. (a) Low-temperature ^{23}Na MAS NMR spectra of $Na_{3-2x}Ca_xPS_4$. Line shapes have been analyzed in Topspin (Bruker) with the software package "sola". At −60 °C, we clearly observe three distinct lines that contribute to the total NMR signal. The spectra were referenced to the ^{23}Na signal of a solid sample of NaCl. (b) Relative area fractions of the three different contributions to the total NMR signal, normalized to the complete area of each ^{23}Na spectrum. (c) Relative area fraction of the three different contributions in each spectrum referenced to the, respective, relative areas of tetragonal Na_3PS_4.

Theoretical studies on Ca-doped Na_3PS_4 suggest lower formation energies when comparing cubic with tetragonal Na_3PS_4. The difference, however, turned out to be quite small (0.03 eV); low dopant levels were not tested.[36] Here, our experimental findings contradict these theoretical results as the

https://doi.org/10.1021/acs.chemmater.3c02874
Chem. Mater. XXXX, XXX, XXX−XXX

sample with $x = 0.0675$ clearly crystallizes with tetragonal symmetry.

To study the effects of processing conditions and structure in Na_3PS_4 in more detail, we synthesized the cubic phase of Na_3PS_4; see the top of Figure 2a. To hinder the cubic-to-tetragonal phase transformation from taking place, the milled sample was annealed at only 250 °C, that is, 450 °C lower than the annealing temperature of the other samples. Accordingly, the broader reflections as compared to the other samples reflect the remaining disorder and distortion introduced through the heavy mechanical treatment. The overall characteristic mimics the reference pattern of cubic Na_3PS_4; however, the broad reflections prevent a clear-cut assignment. Fortunately, the XRD pattern does not point to a strong contamination by starting materials or by crystalline side products. We have to keep in mind that all reflections from the Ca^{2+} source, CaS, overlap with those of Na_3PS_4 because of the similar crystal symmetries.[39]

Consequently, another technique needs to be applied to characterize local structures and to verify successful doping. To analyze whether the local environment of P changes upon Ca incorporation, we used ^{31}P (spin quantum number $I = 1/2$) MAS NMR to study the samples further; see the spectra of Na_3PS_4 and $Na_{2.73}Ca_{0.135}PS_4$ shown in Figure 2b. In Na_3PS_4, the P^{5+} cations occupy only a single crystallographic site. The, respective, MAS NMR spectra are mainly composed of a single line representing the symmetric PS_4^{3-} units in the structure.[40] We observe a similar ^{31}P signal for our undoped tetragonal sample with a minor impurity, shown by the asterix in Figure 2. Besides some low-intensity signals, at a sufficiently high field of 14 T, we resolve a shoulder for the Ca-doped $Na_{2.73}Ca_{0.135}PS_4$ sample at the upfield side. The phosphorus ions in the structure are surrounded by sulfur in the first coordination shell of the PS_4 units, while the Na^+ ions form the second coordination sphere and, in the case of a doped sample, also Ca^{2+} ions. The heavier Ca^{2+} ions result in a larger shielding effect and, thus, a lower local magnetic field. Hence, an upfield shift of the ^{31}P NMR signal is expected. As the amount of Ca^{2+} ions incorporated is quite low in the present case, only a small shift is expected for the sample with $x = 0.135$. Indeed, the main ^{31}P signal reveals a shoulder whose position is shifted by only 0.8 ppm toward lower parts per million (ppm) values. We interpret this shift as an evidence for the successful doping with Ca ions.

In addition to ^{31}P MAS NMR, ^{23}Na ($I = 3/2$) NMR spectroscopy serves as an even more direct tool to study local structures. Figure 3 shows the corresponding variable-temperature NMR spectra of $Na_{2.73}Ca_{0.135}PS_4$ recorded under MAS and for static conditions, that is, without spinning the sample. At sufficiently high spinning speeds, (anisotropic) magnetic dipolar interactions and first-order electric quadrupolar couplings are largely eliminated. In addition, the MAS NMR spectra were recorded at a high magnetic field of 19.9 T as compared to only 7 T for the static spectra, resulting in an overall narrowing of the lines by a factor of 10. While the line shape at room temperature is rather similar under static and under MAS conditions, significant differences appear when lowering the temperature. In contrast to the ^{23}Na NMR spectra recorded without spinning, those acquired at a rotation frequency of 25 kHz and at sufficiently low temperatures reveal distinct spectral components: at −60 °C, the overall ^{23}Na NMR line of $Na_{2.73}Ca_{0.135}PS_4$ is in fact composed of three different signals (see the analysis below).

To investigate the evolution of these spectral components in more detail, we recorded high-resolution ^{23}Na NMR spectra at temperatures down to −60 °C for all three $Na_{3-2x}Ca_xPS_4$ samples with $x = 0$, 0.0675, and 0.135; see Figure 4a. We used the "sola" software package within Topspin to fit and deconvolute the overall NMR signal. The best deconvolution suggests that three quadrupolar sites contribute to each spectrum. Considering the data from XRD, the Ca-doped samples could be understood as mixtures of cubic and tetragonal phases. Importantly, ^{23}Na MAS NMR shows that also the NMR signal belonging to the Ca-free sample ($x = 0$), exhibiting supposedly only tetragonal symmetry, is composed of three NMR lines.

As mentioned above, first-order electric quadrupolar interactions are eliminated by fast MAS, but second-order coupling cannot be fully removed by MAS and results in broadened resonances. This broadening effect in the presence of various quadrupolar lines in combination with fast exchange processes significantly complicates the model-free interpretation of ^{23}Na NMR spectra, especially in the case of NMR lines with similar isotropic chemical shifts.[41] As is shown in Figure 3a, cooling the sample down to sufficiently low temperatures freezes the rapid ionic movements of the Na^+ ions. Consequently, motion-controlled averaging of magnetic and electric interactions through rapid ionic movements of the Na ions is partly eliminated. Under such conditions, the low-T NMR spectra reveal the different contributions to the overall ^{23}Na NMR signal without being fully controlled any longer by dynamic averaging effects.

Our analysis yields that the quadrupolar coupling constants, C_Q, characterizing the distinct NMR lines were rather high for all three sites. C_Q ranges from 2.4 to 2.6 MHz, matching the results for the Na sites in tetragonal Na_3PS_4 as observed earlier by Feng et al.[42] The very similar values for both the C_Q values and the isotropic chemical shifts δ_{iso} indicate a similar chemical environment and crystallographic symmetry for the three Na sites in Na_3PS_4. In general, when dealing with an axially symmetric electric field gradient (EFG) at the nuclear site, the asymmetry parameter η is ∼0.[43] Here, lines 1−3 (see Figure 4a) can be well simulated with almost vanishing η values, meaning that the surrounding electric charge distributions, and thus the corresponding EFGs, are highly symmetric, i.e., we do not find evidence for largely distorted local coordination environments.

In Figure 4b,c, we plotted the area fractions of the three different NMR signals relative to the total ^{23}Na signal and to the relative areas in the reference sample, that is, Ca-free Na_3PS_4. Na_3PS_4 shows the largest area for the most downfield signal 1. While for the sample with $x = 0.0675$ both the intensities for signals 2 and 3 increase, for the sample with highest dopant level ($x = 0.135$) only, signal 2 rises in intensity with reference to Na_3PS_4. As this sample, according to XRD, shows the most cubic character, peak 2 might be associated with a symmetry that is closest to cubic.

A second more likely scenario is, however, the following. Signals 1 and 3 represent the two magnetically and crystallographically inequivalent sites in tetragonal Na_3PS_4. Signal 2, appearing between signals 1 and 3, is an overlapping or dynamically coalesced NMR line shape caused by the rapid exchange processes of the Na^+ ions represented by signals 1 and 3. Accordingly, the exact shape of NMR signal 2 cannot be accessed due to the strong overlap with the other signals; here, this results in fitting values with significant Gaussian broadening for this signal. For the sample with $x = 0.135$, this coalescence

https://doi.org/10.1021/acs.chemmater.3c02874
Chem. Mater. XXXX, XXX, XXX−XXX

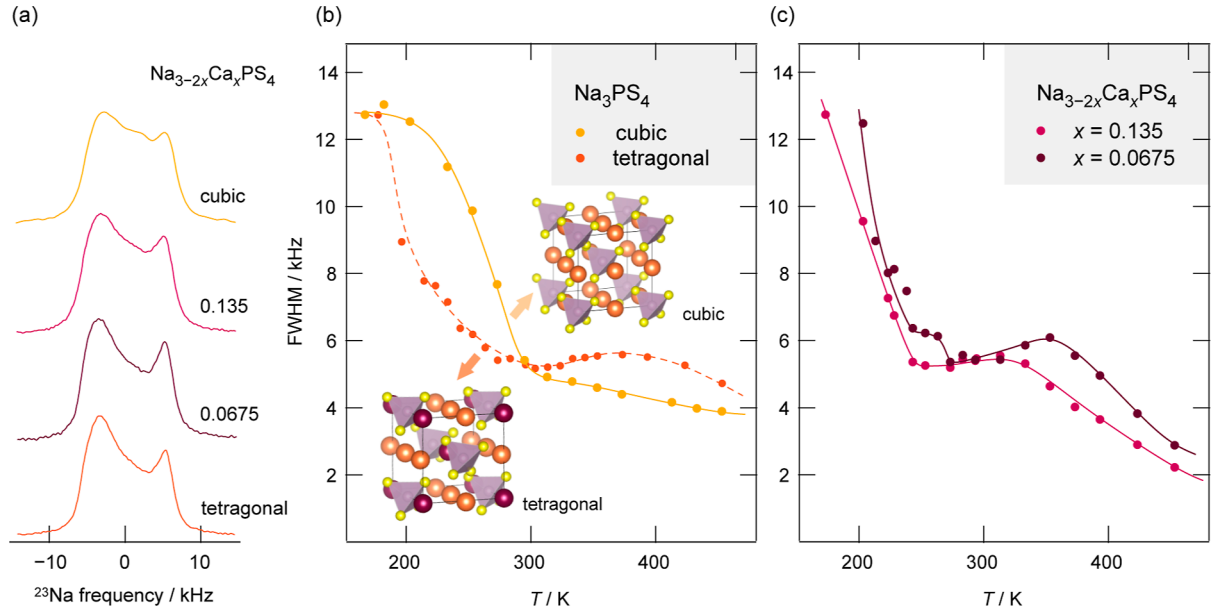

Figure 5. (a) Static ^{23}Na NMR lines of $Na_{3-2x}Ca_xPS_4$ recorded at −100 °C (the exact temperature ranged from −96 to −104 °C). (b,c) Evolution of the overall NMR line width, full width at half-maximum (FWHM), as a function of temperature. While for the undoped, cubic sample the line widths reach its narrowing limit at approximately 300 K, the plots of the samples with $x > 0$ [see (b)] show a second narrowing step at higher temperature. Such a stepwise narrowing behavior is also seen for the tetragonal sample. Dashed and solid lines are drawn as guides to the eye.

effect is most advanced pointing to a higher diffusivity of the Na^+ ions in this sample as compared to the undoped sample, for instance.

To quantify this Na^+ hopping process at −60 °C, we estimated the corresponding exchange rate from the spacing between signals 1 and 3 on the frequency axis. The difference δ_{iso} between the two lines is approximately ν = 1850 Hz, see the top of Figure 4c. This value roughly translates into a hopping rate $1/\tau_{ex}$ of Na^+ at −60 °C of approximately 2000 s^{-1}; hence, the Na^+ residence time at temperatures as low as −60 °C is shorter than 1 ms. Let us note that jumps between equivalent Na sites cannot be seen by MAS NMR. Hence, NMR is just sensitive to a part of the exchange processes taking place in Na_3PS_4. To characterize total ion dynamics, we further studied the samples by ^{23}Na NMR SLR measurements and (broadband) conductivity spectroscopy.

For comparison with our NMR spectra, Feng et al.[42] presented ^{23}Na NMR spectra at a high magnetic field of similar magnitude for Cl-doped $Na_{3-y}PS_{4-x}Cl_x$. They detected up to four different Na^+ sites at 19 T and assigned two signals with high quadrupolar coupling constants, in the range of 2 MHz, to Na^+ located on tetragonal sites, suggesting that such high C_Q values point to an asymmetric structural environment. Additionally, they found two signals with a chemical shift anisotropy $\Delta\delta$ of 10 and 20 ppm and $C_Q \sim 0$, which they assigned to Na ions close to the Cl dopants or located in the direct vicinity of sodium vacancies. Here, these additional lines with significantly different chemical shifts have not been observed in our ^{23}Na NMR measurements on Ca-doped Na_3PS_4. We should note that at room temperature, the Na^+ ions in Na_3PS_4 are expected to be highly mobile with respect to the NMR frequency scale. Hence, we believe that it seems to be very unlikely to see such noncoalesced NMR lines in the presence of rapid Na^+ motions in Na_3PS_4 unless a non-negligible fraction of the Na ions does not participate in overall Na-ion transport. In the present case, we do not find any evidence for such "trapped" vacancies as suggested by Feng et al.[42] Instead, while the low-T ^{23}Na MAS NMR lines labeled 1 and 3 reflect the two regularly occupied Na positions (Na1 and Na2) in tetragonal Na_3PS_4, we think that signal 2 is simply a coalesced signal revealing slow Na-ion exchange processes reaching a hopping rate of 2×10^3 s^{-1} already at −60 °C.

2.2. Na-Ion Dynamics as Seen by NMR. The evolution of the NMR shape and line width, if recorded under static conditions, is a perfect tool to measure element-specific ion dynamics. In general, magnetic dipolar and electric quadrupolar interactions are used to follow their motion-controlled averaging with increasing temperature. The static ^{23}Na NMR lines of $Na_{3-2x}Ca_xPS_4$ recorded at −100 °C are shown in Figure 5a. At this temperature, the overall NMR line width Δ_M of the four different samples was approximately 13 kHz. In Figure 5b, the evolution of this width [full width at half-maximum (FWHM)] is plotted as a function of temperature. While the onset of overall line narrowing is shifted toward higher T for the disordered, cubic Na_3PS_4 sample (x = 0), the dependence of Δ_M on temperature for the other samples looks quite similar. For the cubic sample, Δ_M starts to reach the limit of extreme narrowing at approximately 400 K. This residual line width is determined by any nonaveraged interactions and the inhomogeneity of the external magnetic field B_0.[44]

For quadrupolar nuclei with a relatively large quadrupole moment, such as ^{23}Na, the complexity of the line shape adds a moment of inaccuracy to this fwhm analysis. When coming from low temperatures, we observe that Δ_M of the series $Na_{3-2x}Ca_xPS_4$ reaches a temperature-independent region at intermediate T, as is indicated by the shaded area in Figure 5b. While Δ_M of the cubic sample already reaches the narrowing limit, the other samples show a second narrowing step starting around 350 K that is most pronounced for the Ca-doped samples. Apparently, the Na ions have access to at least another, if not multiple, exchange processes, allowing for further averaging of the residual spin interactions. This peculiar characteristic can also be observed in ^{23}Na NMR spin−lattice relaxation (see below).

https://doi.org/10.1021/acs.chemmater.3c02874
Chem. Mater. XXXX, XXX, XXX−XXX

In Figure 6, the ^{23}Na NMR SLR rates T_1^{-1} recorded in the so-called laboratory frame[45] are plotted as $log_{10}(T_1^{-1})$ versus the inverse temperature $1/T$. Over the temperature range covered, only the so-called low temperature flanks of the characteristic $T^{-1}(1/T)$ rate peaks are observed for all samples. In this temperature regime, the mean jump rate τ^{-1} of the Na^+ ions, which is of the same order of magnitude as the motional correlation rate τ_c^{-1}, is lower than the angular Larmor frequency ω_0.[46] In this limit the rate, $1/T_1$ is sensitive to local hopping processes rather than to long-range ion transport. Dynamic parameters describing the latter would govern the high-T side of a given rate peak, for which $\omega_0\tau_c \ll 1$ holds. In the low-T limit, the slope is, however, mainly affected by the elementary steps of ion hopping. As compared to the situation at the peak maximum ($\omega_0\tau_c \approx 1$),[46−48] at temperatures well below this maximum, only a few jumps are detected within the time window, $1/\omega_0$, set by the NMR experiment, i.e., T_1^{-1} is predominantly governed by the most probable hopping processes. In the case of a heterogeneous, disordered potential landscape, Na^+ exchange between two minima connected by rather low local barriers belongs to this group of motional processes. Hence, for a material with complex ion dynamics, the slope in the limit $\omega_0\tau_c \gg 1$ of a given $T_1^{-1}(1/T)$ rate peak is determined by a *subset* of local exchange processes including within-site motions as well as (correlated) forward and backward jumps. The combined influence of correlation effects and structural disorder may reduce this slope even further.[47,49]

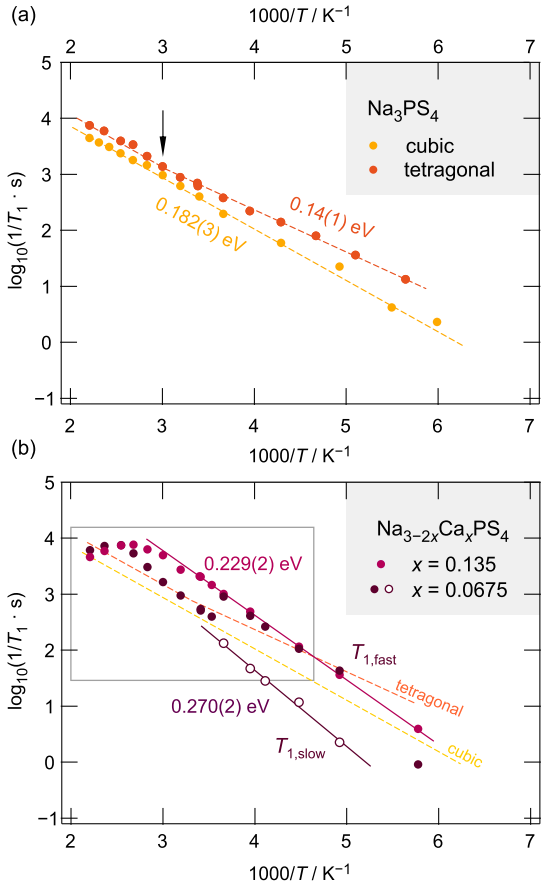

Figure 6. (a) ^{23}Na NMR SLR (spin-lattice relaxation) rates $1/T_1$ ($\omega_0/2\pi$ = 79.39 MHz) for tetragonal Na_3PS_4 and the cubic modification that has been prepared by ball milling and a subsequent soft annealing step. The latter sample is structurally disordered as evidenced by XRD. Dashed lines represent Arrhenius fits, and the values indicate activation energies of this so-called low-T flank. (b) ^{23}Na NMR SLR $1/T_1$ rates recorded under the same conditions as in (a) but for the Ca-bearing samples, as indicated. At lower temperatures, two rates are found for $Na_{3-2x}Ca_xPS_4$ with x = 0.0675 (empty circles, see also Figure 7).

Starting with the disordered, cubic sample (Figure 6a), we see a steadily increasing T_1^{-1} rate whose temperature dependence is characterized by an activation energy E_a of 0.182(3) eV. The NMR SLR rate of tetragonal Na_3PS_4 shows a similar behavior with slightly higher values for T_1^{-1}; the slope yields an activation energy of only 0.14(1) eV (Figure 6). For comparison, Huang et al.[36] calculated barriers of approximately 0.2 eV. As mentioned before, we have to note that motional correlation effects affect the slopes in this limit causing a lower slope for the low-T flank than expected. Hence, the different slopes could reflect the degree of correlation effects affecting short-range ion dynamics in Na_3PS_4. Alternatively, the T_1^{-1} rates belonging to tetragonal Na_3PS_4 reveal a kink near 330 K. We cannot exclude that a superposition of different relaxation processes, that is, faster and slower ones, leads to such a behavior. Similar shoulders, but much more pronounced, have also been observed for other Na-ion conductors.[38,50] Nevertheless, for the Ca-bearing samples, the NMR SLR responses turned out to be quite different.

Beginning with $Na_{2.73}Ca_{0.135}PS_4$ (Figure 6b), we observe a steeper slope of the $T_1^{-1}(1/T)$ flank resulting in E_a = 0.229(2) eV. Again, less-correlated motions in materials with a larger number of vacant sites could be responsible for this increase in slope. In this sense, the activation energy of E_a = 0.229(2) eV has to be interpreted as an apparent value. Most importantly, the NMR SLR rates of $Na_{2.73}Ca_{0.135}PS_4$ pass through a maximum at T_{max} = 373 K, indicating Na^+ hopping processes on the local length (or time) scale that even exceed those present in tetragonal Na_3PS_4 as no such maximum is seen up to T = 450 K for the Ca-free sample. As we will see below, higher activation energies and higher Arrhenius prefactors, i.e., attempt frequencies, ensure that such a rate maximum in $1/T_1$ is already seen for $Na_{2.73}Ca_{0.135}PS_4$ at 373 K.

The appearance of this rate maximum allows us to directly determine an average Na^+ jump rate $1/\tau$(373 K) of 2.0×10^9 s^{-1} (Figure 7). For comparison, Moon et al. reported T_{max} = 360 K and E_a = 0.346 eV for $Na_{2.73}Ca_{0.135}PS_4$.[33] Since the diffusion-induced rate maximum $T_1^{-1}(1/T)$ of $Na_{2.73}Ca_{0.135}PS_4$ turns out to be relatively broad, we cannot exclude that it is a superposition of several relaxation process running in parallel. Such a distribution would be in line with the observation of a stepwise decay of the NMR line width as discussed above for this sample.

The diffusion-induced T_1^{-1} NMR SLR rates of the Ca-doped sample $Na_{2.865}Ca_{0.0675}PS_4$ deviate from the responses seen for the other samples (Figure 6b); it somehow takes an intermediate position in terms of dynamic parameters seen by NMR. At temperatures below 0 °C, the underlying magnetization transients from which the rate T_1^{-1} is extracted exhibit a double-exponential behavior leading to two rates $T_{1,fast}^{-1}$ and $T_{1,slow}^{-1}$. While $T_{1,fast}^{-1}$ coincides with T_1^{-1} of $Na_{2.73}Ca_{0.135}PS_4$, the rates $T_{1,slow}^{-1}$ follow an Arrhenius line that is characterized by E_a = 0.270(2) eV (Figure 6b). Obviously, only a part of the Na ions in $Na_{2.865}Ca_{0.0675}PS_4$ have access to a fast diffusion process, and the other part determines the rate peak which finally appears at T_{max} = 417 K; see Figure 7. The more the rate peak is shifted toward higher T, the slower the diffusivity of the sample at temperatures lower than T_{max}.

https://doi.org/10.1021/acs.chemmater.3c02874
Chem. Mater. XXXX, XXX, XXX−XXX

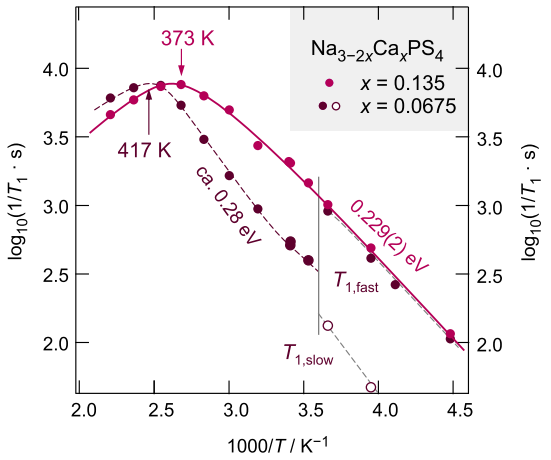

Figure 7. Magnification of the ^{23}Na SLR rates of $Na_{3-2x}Ca_xPS_4$ shown in Figure 6b. Dashed lines show Arrhenius fits; the solid line serves as a guide to the eye. The rates belonging to $Na_{2.73}Ca_{0.135}PS_4$ pass through a maximum at 373 K, from which a mean jump rate 2.0×10^9 s^{-1} can be directly determined. The NMR SLR response of $Na_{2.865}Ca_{0.0675}PS_4$ turned out to be more complex as two SLR rates need to be taken into account to fully describe longitudinal recovery of the magnetization. See the text for further explanation.

To see whether the differences in local ion dynamics have an impact on long-range ion transport, the samples have been investigated by electrical measurements. In the following section, we used both (i) conductivity spectroscopy and (ii) electric modulus spectroscopy to characterize the overall electric transport in Na_3PS_4. Polarization measurements in the (true) direct current (dc) mode helped us to estimate the upper limit of electronic contributions to the overall (or total) electric conductivity.

2.3. Ion Dynamics on a Long-Range Scale. To shed light on the macroscopic transport properties of $Na_{3-2x}Ca_xPS_4$, we investigated the samples by alternating current (ac) conductivity spectroscopy. In Figure 8, the real part of the complex conductivity σ' of tetragonal Na_3PS_4 and Ca-bearing $Na_{3-2x}Ca_xPS_4$ ($x = 0.135$) is shown as a function of frequency ν for temperatures ranging from −120 °C up to 180 °C. The isotherms of the other two samples are shown in Figure S1a. We identify the classical three regimes governing the isotherms. The polarization regime at low frequencies (I) passes into the frequency-independent conductivity plateau (II) that is finally discharged into the so-called dispersive part (III) characterizing localized electric fluctuations.

Reading off the conductivities in region II leads us to the Arrhenius plot where $\sigma'T$ is plotted vs $1/T$; see below. At this point, we cannot exclude that σ' referring to region II is, however, additionally affected by grain boundary resistances, that is, representing the overall (ionic) conductivity. As we will show below, the electronic conductivity σ_{eon} turned out to be much lower. In general, in solid oxide electrolytes, typically the grain boundary resistance significantly decreases the overall ionic conductivity. This effect is less pronounced in sulfides; however, also these softer-textured materials show differences in ionic transport in the bulk and grain boundary regions.[51] Even here, the contribution of different processes in Na_3PS_4 can be shown in a number of aspects.

To test to which extent grain boundary contributions affect region II, we included the electric modulus $M''(\nu)$ peaks in Figure 8. The amplitude of a given M'' peak is inversely proportional to the capacitance C and is thereby especially sensitive to bulk phenomena.[52] Here, for the tetragonal sample (see Figure 8), it can be clearly seen that the position of the peak on the frequency scale does not coincide with the well-resolved σ'-plateaus (II.). The same shift is seen for the disordered cubic sample as well as for the sample with $x = 0.0675$ (see Supporting Information, Figure S1). Hence, we conclude that apart from dynamic processes contributing to region II, the processes taking place in the bulk regions exclusively determine the $M''(\nu)$ peaks.

This view is fully supported by the fact that $\sigma'(\nu)$ of $Na_{2.73}Ca_{0.135}PS_4$, see Figure 8b, reveals a stepwise increase of σ' clearly leading to two plateau regions labeled A and B, and leading to two distinct conductivity values (see below). The main modulus peak points to region B. In the other samples, these regions (A and B) are merged such that a separation is no longer possible. However, double-logarithmic plots of $M''(\nu)$

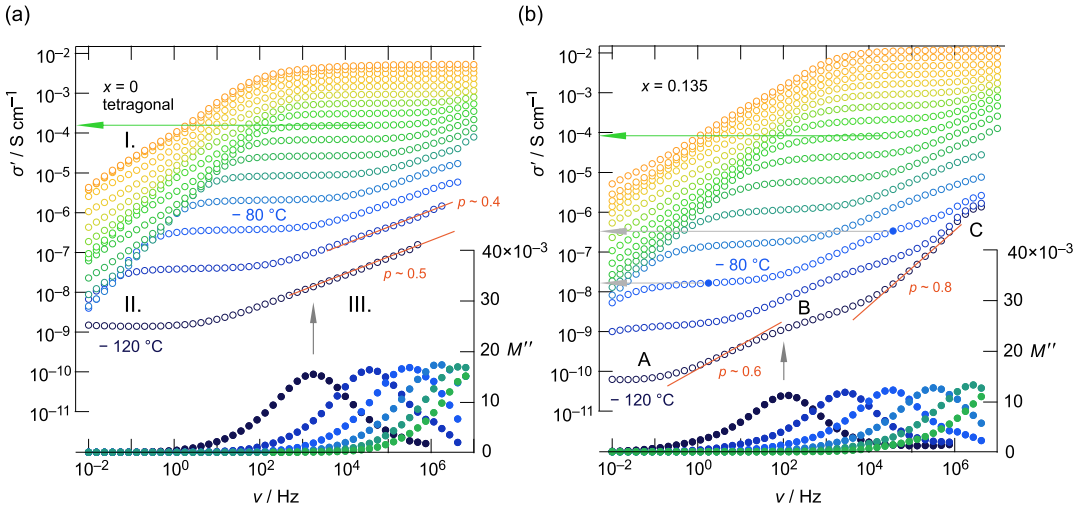

Figure 8. Conductivity isotherms $\sigma'(\nu)$ showing the real part of the conductivity of $Na_{3-2x}Ca_xPS_4$ [(a) $x = 0$ and (b) $x = 0.135$] as a function of frequency ν. Isotherms were recorded from −120 to 180 °C in steps of 20 K. On the right axis, the imaginary part of the electric modulus M'' is plotted vs ν. The modulus peaks shown are sensitive to electrical fluctuations in the bulk regions. At higher T, the peaks are outside the frequency region of our setup. Only for $Na_{2.73}Ca_{0.135}PS_4$, a clear separation of two contributions is seen in $\sigma'(\nu)$. See the text for further details.

https://doi.org/10.1021/acs.chemmater.3c02874
Chem. Mater. XXXX, XXX, XXX−XXX

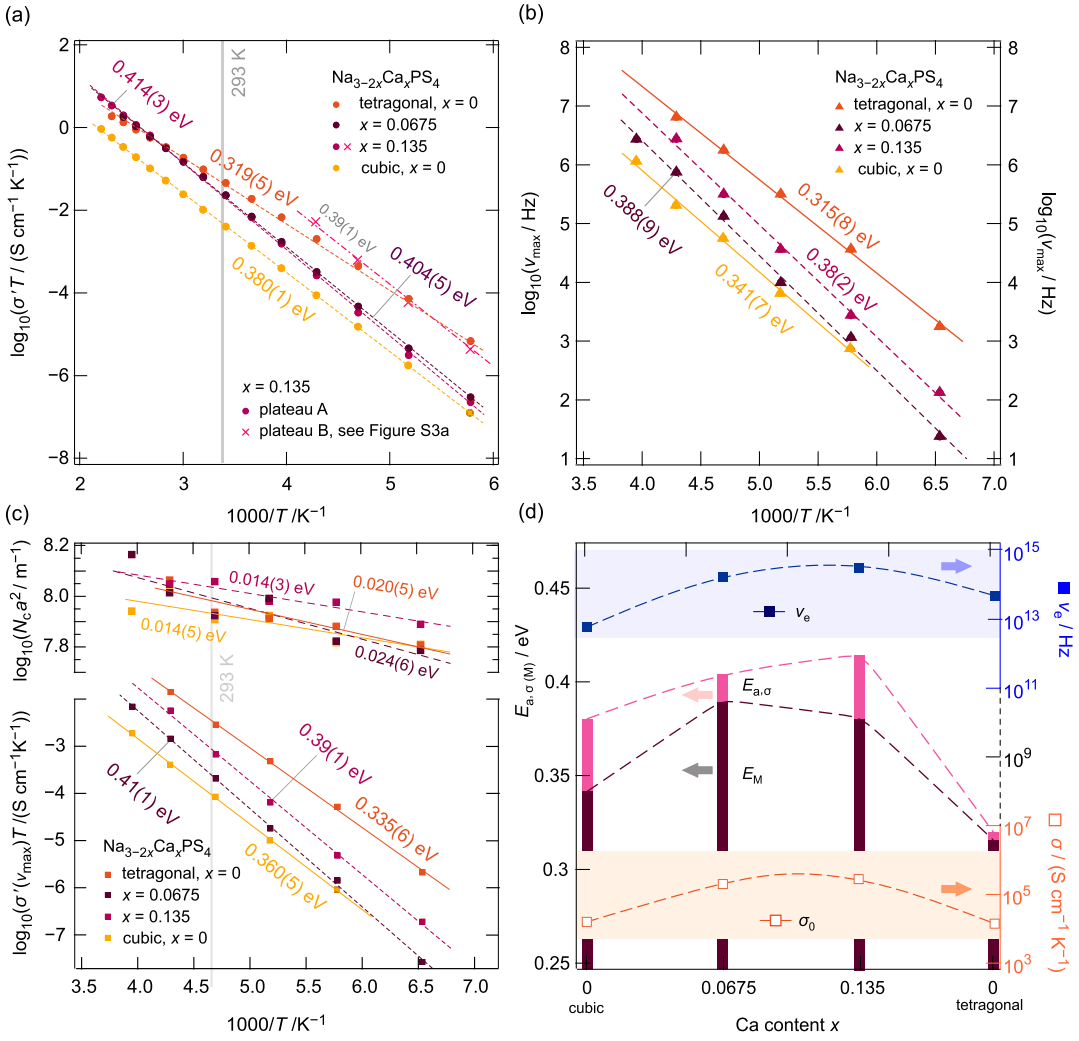

Figure 9. (a) Arrhenius plot showing the dependence of $\sigma' T$ as a function of the inverse temperature of the $Na_{3-2x}Ca_xPS_4$ samples; see key. Dashed lines refer to linear fits; activation energies $E_{a,\sigma}$ are indicated. For $Na_{2.73}Ca_{0.135}PS_4$, two values per temperature are included as the associated isotherms $\sigma'(\nu)$ show two plateau regions, A (•) and B (×). (b) Temperature dependence of the hopping rate ν_{max} is shown, as derived from the electric modulus peaks displayed in Figure 8. (c) Top: variation of the charge carrier concentration N_c, shown as $N_c a^2$ with a being the mean hopping distance. Bottom: temperature dependency of the conductivity σ' read off at ν_{max}, i.e., at the location of the M'' peaks on the frequency scale. Dashed and solid lines are linear fits yielding the activation energies indicated. (d) Summary of the dynamic parameters from our electrical analysis: $E_{a,\sigma}$ denotes the activation energy from $\sigma' T(1/T)$ (regions II and A) and E_M refers to the activation energy as deduced from the electric modulus M'' peak analysis; ν_e is the effective attempt frequency and σ_0 denotes the Arrhenius prefactor of $\sigma' T(1/T)$. The dashed lines serve as guides to the eye.

clearly show two contributions to the overall shape of $M''(\nu)$, that is, reflecting the two-step increase seen for $\sigma'(\nu)$; see Supporting Information, Figure S2. While these two modulus peaks are separated by at least 2 orders of magnitude on the frequency axis, the corresponding σ' values differ by only 1 order of magnitude, as is illustrated in Figure 8b. Obviously, the effective charge carrier concentration N_c, to which σ' is proportional, is different for the two processes.

The fact that region II is composed of several processes is further underpinned by the fact that regions II and III cannot be well approximated with a single Jonscher-type power law.[53] Here, we analyzed the dispersive parts of the isotherms with power laws of the following form.[54]

$$\sigma'(\nu) = \sigma'(\nu \to 0) \times \left[1 + \left(\frac{\nu}{\nu_H}\right)^p\right] \quad (1)$$

p represents the power law exponent and ν_H is the so-called crossover frequency connecting region II, with region III. Reasonable fits are only possible for the Ca-bearing $Na_{2.73}Ca_{0.135}PS_4$ sample yielding exponents p ranging from 0.7 to 0.8. These values point to 3D charge transport[55] as also suggested by others for Na_3PS_4.[31,35,42] For the other samples, the seemingly lower exponents when parametrizing the complete isotherms result from a depressed slope originating from "hidden" type-II plateaus in the dispersive regions.

Finally, by analyzing the impedance data within the frame of the Nyquist plots, the overall response can only be understood as a combination of at least two depressed semicircles; see Supporting Information, Figure S3a. As an example, parametrizing the Nyquist location curve of the disordered, cubic Na_3PS_4 sample with two circuit elements results in electric capacitances ranging from 24 to 800 pF. These values clearly show that region II comprises both bulk properties (24 pF) and ion-blocking contributions from grain boundary regions (>800 pF).[56]

In summary, considering the features seen from the modulus peaks, the shape and characteristics of the dispersive regions

https://doi.org/10.1021/acs.chemmater.3c02874
Chem. Mater. XXXX, XXX, XXX−XXX

(III) as well as the Nyquist analysis, we believe that several dynamic processes are needed to describe the full responses in both Ca-free and Ca-bearing Na_3PS_4. Only for $Na_{2.73}Ca_{0.135}PS_4$ are these processes distinctly seen even in the $\sigma'(\nu)$ representation; see Figure 8b. Most likely, resistive grain boundary regions lead to an additional drop of the isotherms $\sigma'(\nu)$ in the low-frequency region.

Before discussing the sample-specific $\sigma'T$ values deduced from region II as a function of temperature, we need to determine the contribution of any electronic charge carriers, i.e., other than ionic species, to the total conductivity. For this purpose, we carried out chronoamperometric polarization experiments.[38,57] After polarizing the $Na_{2.73}Ca_{0.135}PS_4$ sample for $t = 45$ h at a potential of $U = 0.1$ V, the current I reached a final value of 98 pA, see Figure S4 in the Supporting Information. This value translates into a specific electronic conductivity σ_{eon} of 8.3×10^{-11} S cm^{-1}. Compared to $\sigma' = 1.36 \times 10^{-5}$ S cm^{-1} (region II), this value is 6 orders of magnitude lower than the total conductivity leading to a transference number t_{Na^+} of almost 1 (0.999994). Accordingly, the electronic contribution to the total electric response in $Na_{3-2x}Ca_xPS_4$ is negligible here.

To determine activation energies that characterize ion transport in Na_3PS_4, we analyzed $\sigma'T$ from region II as well as determined the characteristic electric relaxation frequencies from the modulus peaks $M''(\nu)$. Assuming

$$\sigma'T = \sigma_0(1/T \rightarrow 0)\exp\frac{E_{a,\sigma}}{k_BT} \tag{2}$$

with k_B being Boltzmann's constant, $\sigma'T$ is expected to follow a linear behavior when plotted as a function of $1/T$. The corresponding Arrhenius lines for $Na_{3-2x}Ca_xPS_4$ are shown in Figure 9a.

While the disordered, cubic phase prepared through milling and the soft annealing step shows the lowest (total) conductivity in our series, the tetragonal, undoped phase reveals the highest ionic conductivity at room temperature. However, at temperatures higher than 120 °C, the ionic conductivity of the Ca-doped samples exceeds that of undoped, tetragonal Na_3PS_4. This behavior mirrors the mutual influence of activation energies E_a and Arrhenius prefactors σ_0 on ionic transport over such a large temperature range. As mentioned above, for cubic $Na_{2.73}Ca_{0.135}PS_4$, two distinct $\sigma'T$ values are obtained referring to regions A and B. The values of B, corresponding to lattice ion dynamics, are at least 1 order of magnitude higher than those belonging to A and, thus, they are comparable to that from region II of Ca-free tetragonal Na_3PS_4 at low temperature (see cross symbols in Figure 9a).

To extract information on pure *bulk* ionic conductivities also for the other samples, we used the characteristic frequency ν_{max} of the main peak of M'' to read off $\sigma'(\nu_{max})$, which we analyzed in the frame of an Arrhenius plot; see Figure 9c. As expected, $\sigma'T$ of tetragonal Na_3PS_4 is even higher than $\sigma'T$ of region B, revealing the superior properties of this sample in terms of bulk ion conductivity. Only at high temperatures, $\sigma'T$ belonging to region B of the isotherms of $Na_{2.73}Ca_{0.135}PS_4$ will substantially exceed $\sigma'T$ of the tetragonal sample (see Figure S3b). Both a higher value of $E_{a,\sigma'}(\nu_{max})$ (0.39 eV vs 0.34 eV) and a larger prefactor σ_0 cause this behavior. Moreover, the activation energies derived from the bulk regions (see Figure 9c) are slightly lower compared to that describing the total conductivity, cf. Figure 9a. This finding points to facile ion diffusion within the crystallite regions and an ion-blocking character of the grain boundary zones, which lead to a lower total conductivity.

In addition to investigating $\sigma'T$ (regions II and A) and $\sigma'(\nu_{max})T$, we directly looked at the temperature dependence of the modulus peak frequencies ν_{max}, see Figure 9b, to understand the bulk ion dynamics further. For ν_{max}, we again assume Arrhenius behavior

$$\nu_{max} = \nu_e\exp\frac{E_M}{k_BT} \tag{3}$$

ν_{max} is considered to be on the same order of magnitude as the hopping rate of the mobile ions ν_H. Since it is a temperature-activated property, it is associated with an effective attempt frequency ν_e and an activation energy E_M related to charge carrier migration. As is shown in Figure 9b, in principle, the same trend as for $\sigma'T$ is obtained. Again, at sufficiently high temperatures, the higher activation energy of $Na_{2.73}Ca_{0.135}PS_4$ (0.38 eV) combined with a higher prefactor ν_e (see Figure 9d) will lead to electrical relaxation frequencies clearly exceeding those of tetragonal Na_3PS_4. In agreement with the trend seen for $\sigma'T$, increasing disorder in cubic Na_3PS_4 seems to be less favorable for ion migration as the sample prepared by milling *and* annealing at 250 °C has to be characterized by the lowest conductivities.

Besides the activation energy and the Arrhenius prefactor,[58] another crucial parameter determining ionic transport is the charge carrier concentration N_c. Combining the Nernst–Einstein equation,[59] relating the ionic mobility with the diffusion coefficient and N_c, with the Einstein–Smoluchowski relation[60,61] describing the diffusion coefficient by means of the jump distance a and the jump rate ν_H, we obtain the following expression. Strictly speaking, this expression is only valid for the dilute regime of charge carriers with no strong correlation effects

$$N_c \times a^2 = \frac{k_BT}{e^2\gamma} \times \frac{\sigma'(\nu_{max})}{\nu_H} \tag{4}$$

Here, e is the elemental charge, and γ is a geometrical factor related to the dimensionality of the diffusion process. The product of N_c with the hopping distance squared a^2 is shown on top of Figure 9c. Since $N_c \propto \sigma'/\nu_H$, this parameter depends on temperature if the difference between total and migration activation energy, so-called activation energy for charge carrier creation, $E_c = E_{a,\sigma'(\nu_{max})} - E_M \neq 0$. As mentioned above, $E_{a,\sigma'(\nu_{max})}$ means here that it refers to the $\sigma'(\nu_{max})T(1/T)$ isotherms. We find that the cubic, disordered sample and the cubic-appearing $Na_{2.73}Ca_{0.135}PS_4$ show a weak change of N_c with temperature: E_c is given by approximately 0.014 eV, which is similar to that of other compounds such as glasses.[62] For the samples with tetragonal symmetry, E_c does not change much and amounts to 0.02 eV. In crystalline samples, such a temperature-dependent charge carrier concentration is usually related to the existence of "trapped" ions.[62,63] In Figure S3b, we analyzed N_c of region II, which is not only affected by bulk but also by the influence of grain boundary effects. Although fraught with difficulties, one might speculate that especially for the sample with a higher amount of Na vacancies ($x = 0.135$), a situation with fewer trapped Na ions is created. Indeed, N_ca^2 of $Na_{2.73}Ca_{0.135}PS_4$, which corresponds to region A, shows a rather temperature-independent behavior.

Moon et al.[33] addressed the aspect of mobile and trapped ions by calculating mean square distances of the mobile Na ion by molecular dynamics simulations. They found the role of dopant

https://doi.org/10.1021/acs.chemmater.3c02874
Chem. Mater. XXXX, XXX, XXX−XXX

ions to be secondary as a Na-deficient phase of $Na_{2.875}PS_4$ showed higher mean-square displacement values compared to a Ca-doped structure with the same vacancy concentration. Indeed, as we even see rather high hopping rates, ν_H, for tetragonal Na_3PS_4, the vacancy concentration cannot be the only crucial parameter. We need to consider structure and crystallinity as a result of processing conditions equally as influential regarding the ion-hopping processes in Na_3PS_4.

In Figure 9d, we summarized the various activation energies and prefactors for the different samples studied. A complete summary of all fitting parameters from Figure 9 can be found in Tables S1 and S2. The superiority of tetragonal Na_3PS_4 over the other samples at ambient temperature lies in the very low activation energies for both total conductivity $\sigma'T$ and electrical relaxation frequency ν_H. Higher activation energies seen for cubic, disordered Na_3PS_4 are most likely a consequence from remaining defects and strain introduced by ball milling, which were not removed by the annealing step at 250 °C.[32]

The prefactors ν_e and especially σ_0 of tetragonal Na_3PS_4 turned out to be lower than those found for samples with dopant levels $x > 0$. By comparing tetragonal Na_3PS_4 with $Na_{2.73}Ca_{0.135}PS_4$, we see that σ_0 has decreased by 2 orders of magnitude. This decrease is in line with the so-called Meyer-Neldel rule[64] predicting that lower prefactors are associated with lower activation energies.

Interestingly, the relatively high activation energies probed for the Ca-doped samples (Figure 9d) were also observed by Moon et al.[33] According to our ν_H analysis, we believe that the high prefactors σ_0 of these samples do not result from higher charge carrier concentrations but to increased attempt frequencies ν_e since the two vary in a rather similar way from sample to sample; see Figure 9d. Altogether, higher activation energies and larger prefactors are both quantities responsible for the superior performance of the Ca-doped $Na_{3-2x}Ca_xPS_4$ samples at elevated temperatures.

Finally, in order to find out whether the ^{23}Na NMR SLR rates of $Na_{2.73}Ca_{0.135}PS_4$ detect the same dynamic process as seen by electric measurements, we compared the NMR jump rate of $1/\tau(373\ K) = 2.0 \times 10^9\ s^{-1}$ with that of $\nu_H(1/T)$ from impedance spectroscopy after an extrapolation to 373 K. Such an extrapolation yields $3.1 \times 10^9\ s^{-1}$, which is a factor of less than 2 in perfect agreement with $1/\tau(373\ K)$. This striking agreement emphasizes that the rate peak in NMR does in fact mirror the ion dynamics of the overall bulk, although the activation energies of the two methods are affected by further length-scale-dependent parameters (see above). As mentioned above, in the low-T range, E_a of NMR SLR is likely to be influenced by correlation effects yielding apparent values that are lower than expected. Unless the high-T flank of a given NMR SLR peak is accessible, only at the rate maximum, an almost model-independent access to jump rates (and diffusion coefficients) is given.

The motional exchange rate, which has been deduced by ^{23}Na MAS NMR (see above, $1/\tau_{ex} \approx 2 \times 10^3\ s^{-1}$ for $x = 0.135$) underestimates Na^+ diffusivity, as ν_{max} would suggest rates as high as $10^5\ s^{-1}$ at −60 °C for $Na_{2.865}Ca_{0.0675}PS_4$ (Figure 9b). We conclude that also jump processes between (magnetically) equivalent sites, most likely using interstitial positions, contribute to overall ion dynamics in $Na_{3-2x}Ca_xPS_4$ to a non-negligible extent. On the other hand, we believe that also localized (unsuccessful) forward−backward jump processes affect ν_{max}. Such events would hardly manifest as a coalesced line in NMR.

3. CONCLUSIONS

To evaluate the effects of doping and processing conditions on local structure and ion dynamics in sodium thiophosphate Na_3PS_4, we synthesized $Na_{3-2x}Ca_xPS_4$ with different Ca^{2+} dopant levels. Most importantly, even for the Ca-rich sample ($x = 0.135$) showing cubic XRD characteristics, low-temperature ^{23}Na magic angle spinning NMR revealed two Na sites, which are expected for a tetragonal geometry. Hence, on the local, that is, the angstrom scale, tetragonal symmetry is directly probed. A third, Gaussian-shaped NMR line shows exchange processes between the two regularly occupied Na sites. This line points to Na^+ exchange rates with values in the kilohertz range already activated at −60 °C. Electric modulus data does reveal even faster dynamic processes, clearly positioning Na_3PS_4 as an extremely fast ion conductor.

Tetragonal Na_3PS_4 turned out to be a fast ion conductor with a lower conductivity activation energy than those probed for the Ca-bearing samples. The activation energies both for local and (macroscopic) long-range transport in tetragonal Na_3PS_4 are even lower than those in the defect-rich cubic sample. However, at higher T, the conductivity of tetragonal Na_3PS_4 suffers from a lower Arrhenius prefactor. For the disordered cubic sample, we found that the lower crystallinity, resulting from the lower annealing temperature to retain the cubic phase, is detrimental for ionic transport and highlights the importance of processing conditions for the performance of Na_3PS_4 as an ionic conductor.

Interestingly, the incorporation of Ca^{2+} ions leads to an increase rather than a decrease in activation energies seen by both NMR and electrical measurements, that is, on a wide time and length scale. In particular, we observe a diffusion-induced NMR relaxation rate maximum for $Na_{2.73}Ca_{0.135}PS_4$ revealing rather fast Na^+ exchange processes on the angstrom length scale. These processes might be even faster than those in tetragonal Na_3PS_4, where the peak maximum could not be reached up to 450 K.

Relatively high activation energies combined with larger Arrhenius prefactors and attempt frequencies will cause the overall ionic conductivity of vacancy-rich $Na_{2.73}Ca_{0.135}PS_4$ to exceed that of the tetragonal sample at temperatures higher than 350 K. Hence, processing conditions and substitution strategies, as exemplarily studied in the case of Ca doping, will affect a range of length-scale dynamic parameters including the Arrhenius prefactor, in particular. We were able to show that Ca-doping in $Na_{3-2x}Ca_xPS_4$ leads to an increase of the Arrhenius prefactors. The energy barriers for ionic transport are, however, also critically influenced by the processing steps such as the annealing temperature affecting local structure and the overall degree of crystallinity. It turned out that Ca-bearing $Na_{2.73}Ca_{0.135}PS_4$ with local tetragonal symmetry will outperform tetragonal Na_3PS_4 only at elevated T. This fact along with higher attempt frequencies and disorder effects introduced by the doping makes $Na_{2.73}Ca_{0.135}PS_4$ a promising candidate as Na-conducting material.

To conclude, we were able to show that Ca doping in $Na_{3-2x}Ca_xPS_4$ strongly increases prefactors for the diffusional processes, but the energy barriers are also critically influenced by the processing steps like the annealing temperature and the resulting structure and degree of crystallinity. It is crucial to understand all steps along the chain to really tune ionic conductivity in Na_3PS_4 structures. Our study will help in better designing future-related Na-solid electrolyte materials.

https://doi.org/10.1021/acs.chemmater.3c02874
Chem. Mater. XXXX, XXX, XXX−XXX

4. EXPERIMENT

4.1. Preparation of the Samples. For the solid-state synthesis, stoichiometric amounts of Na_2S (Alfa Aesar, no specification on purity), P_2S_5 (Sigma-Aldrich, 99%), and CaS (abcr, 99.9%) were used. For undoped Na_3PS_4, no CaS was used; for the doped samples, the, respective, amount of CaS (0.0675 and 0.135 mol equ.) was used on the expense of Na_2S. The powder was mixed in a zirconia beaker (volume of 45 mL) together with 180 ZrO_2 balls (5 mm diameter) and milled for 20 h at 400 rpm. Three grams of precursor material were used, so the ball-to-powder ratio was 11:1. The resulting powder was pelletized in 5 mm tablets and fire-sealed in Duran glass (for heat treatment below 500 °C) or quartz glass tubes. For cubic Na_3PS_4, the samples were heated to 250 °C (heating rate 50 K/h) and annealed for 12 h, followed by natural cooling. For the tetragonal and the Ca-doped samples, the heat treatment was conducted at 700 °C (heating rate 300 K/h) for 12 h, again followed by natural cooling. All steps were carried out under exclusion of air and moisture.

4.2. X-ray Powder Diffraction. Powder diffractograms were measured using a Rigaku MiniFlex X-ray diffractometer equipped with a Cu X-ray tube with $\lambda_{K\alpha 1}$ = 1.54059 Å and a D/teX Ultra silicon strip detector. The measurements covered a 2θ range staring from 10° to 60°. The scanning speed was 0.1°/s. We used an airtight sample holder by Rigaku for the measurements.

4.3. MAS Nuclear Magnetic Resonance. For enhanced resolution, ^{23}Na spectra of selected samples were measured at an ultrahigh field of 19.9 T corresponding to a Larmor frequency for Na of ν_0 = 224.88 MHz. All spectra were referenced to the ^{23}Na signal of NaCl (0 ppm). Spectra were recorded at four different temperatures reaching as low as −60 °C to improve resolution of the Na lines of Na_3PS_4. The spectra were fitted with TopSpin 4.1.4 using the software package "sola". The ^{31}P spectra were recorded at a magnetic field of 14 T corresponding to a Larmor frequency of 242.9 MHz. The spectra were referenced to 1 M H_3PO_4 using BPO_4 as a secondary reference with the isotropic NMR chemical shift δ at −29.6 ppm.

4.4. NMR SLR Measurements. All samples were fire-sealed in quartz glass tubes under dynamic vacuum to permanently protect them from air or moisture. Measurements were performed with a Bruker Avance III spectrometer that is connected to cryomagnet (Bruker) with a nominal magnetic field of 7.05 T, which corresponds to a ^{23}Na Larmor frequency of 79.39 MHz. We used a commercial Bruker probe with a sample chamber made of Teflon and performed variable-temperature NMR measurements within the temperature limitations of the probe, that is, from −100 °C up to 180 °C. NMR SLR rates in the laboratory frame ($1/T_1$) were determined by the well-known saturation recovery pulse sequence.[65] The lengths for $\pi/2$ pulses ranged from 2.4 to 5.0 μs at power levels of 140−200 W. The magnetization transients were fitted by stretched exponential functions. For the sample with a Ca content of x = 0.0675, a double-exponential behavior was found at temperatures below 10 °C. The logarithm of the rates $1/T_1$ was plotted vs the inverse temperature $1/T$ to construct an Arrhenius plot. Activation energies were derived from the accessible low-T flanks of the NMR SLR rate peaks.

4.5. Conductivity Spectroscopy. For the impedance analysis, the annealed polycrystalline samples were ground in a mortar and then uniaxially cold pressed into pellets of 5 mm diameter with a thickness in the range of 1 mm. The exact height of each sample was determined after the measurement by a micrometer dial gauge with an accuracy of 0.01 mm. The geometry of each pellet was used to calculate and consider the cell stray plus spacer capacities in the impedance data. Both sides of the pellets were sputtered with ion-blocking layers of gold (50−100 nm). We recorded complex impedance data in a frequency range from 10 mHz to 10 MHz. A temperature window from −120 to 180 °C was covered with a set of measurements every 20 K. The measurement device was a Novocontrol Concept 80 broadband analyzer that is operated in combination with a QUATRO cryosystem to precisely control the temperature inside the sample chamber. During the mounting procedure of the sample in the active cell, the sample was exposed to air for a few seconds. During the measurement, the sample is excluded from any reaction with air or moisture because the sample is placed in a constant stream of freshly evaporated N_2.

4.6. Potentiostatic Polarization Measurements. For the Ca-doped sample with x = 0.135, the same pellet used for impedance spectroscopy was studied to determine the electronic conductivity by using a Versa STAT3 potentiostat with a so-called low current interface. We applied a potential U of 0.1 V and left the sample to polarize for a duration t of 45 h until a plateau of the final current signal $I(t \rightarrow \infty)$ was reached.

■ ASSOCIATED CONTENT

Supporting Information

The Supporting Information is available free of charge at https://pubs.acs.org/doi/10.1021/acs.chemmater.3c02874.

Further experimental details and conductivity isotherms, fitting paraments, and Nyquist plots (PDF)

■ AUTHOR INFORMATION

Corresponding Authors

Katharina Hogrefe − *Institute for Chemistry and Technology of Materials, Graz University of Technology, AT-8010 Graz, Austria;* orcid.org/0000-0002-2747-405X; Email: katharina.hogrefe@alumni.tugraz.at

H. Martin R. Wilkening − *Institute for Chemistry and Technology of Materials, Graz University of Technology, AT-8010 Graz, Austria;* orcid.org/0000-0001-9706-4892; Email: wilkening@tugraz.at

Authors

Jana Königsreiter − *Institute for Chemistry and Technology of Materials, Graz University of Technology, AT-8010 Graz, Austria*

Anna Bernroitner − *Institute for Chemistry and Technology of Materials, Graz University of Technology, AT-8010 Graz, Austria*

Bernhard Gadermaier − *Institute for Chemistry and Technology of Materials, Graz University of Technology, AT-8010 Graz, Austria;* orcid.org/0000-0003-2917-1818

Sharon E. Ashbrook − *School of Chemistry EaStCHEM and Centre of Magnetic Resonance, University of St Andrews, St Andrews KY16 9ST, U.K.;* orcid.org/0000-0002-4538-6782

Complete contact information is available at: https://pubs.acs.org/10.1021/acs.chemmater.3c02874

Notes

The authors declare no competing financial interest.

https://doi.org/10.1021/acs.chemmater.3c02874
Chem. Mater. XXXX, XXX, XXX−XXX

■ ACKNOWLEDGMENTS

We thank Emma Borthwick for support during the high-field NMR measurements. We also thank the UK Solid-State NMR Facility for support. The UK High-Field Solid-State NMR Facility used in this research was funded by EPSRC and BBSRC (EP/T015063/1), as well as the University of Warwick including part funding through Birmingham Science City Advanced Materials Projects 1 and 2 supported by Advantage West Midlands (AWM) and the European Regional Development Fund (ERDF). The funding for K. Hogrefe by Stipendien der *Monatshefte für Chemie* is greatly appreciated. We appreciate financial support by the Deutsche Forschungsgemeinschaft (DFG) [WI3600 (4-1 and 2-1)] and by the FFG projects CERES and safeLIB.

■ REFERENCES

(1) Gür, T. M. Review of Electrical Energy Storage Technologies, Materials and Systems: Challenges and Prospects for Large-Scale Grid Storage. *Energy Environ. Sci.* **2018**, *11*, 2696−2767.
(2) Mitali, J.; Dhinakaran, S.; Mohamad, A. Energy Storage Systems: A Review. *Energy Storage Sav.* **2022**, *1*, 166−216.
(3) Krishan, O.; Suhag, S. An Updated Review of Energy Storage Systems: Classification and Applications in Distributed Generation Power Systems Incorporating Renewable Energy Resources. *Int. J. Energy Res.* **2019**, *43*, 6171−6210.
(4) Akinyele, D.; Rayudu, R. Review of Energy Storage Technologies for Sustainable Power Networks. *Sustain. Energy Technol. Assessments* **2014**, *8*, 74−91.
(5) Larcher, D.; Tarascon, J. M. Towards Greener and More Sustainable Batteries for Electrical Energy Storage. *Nat. Chem.* **2015**, *7*, 19−29.
(6) Ding, Y.; Cano, Z. P.; Yu, A.; Lu, J.; Chen, Z. Automotive Li-Ion Batteries: Current Status and Future Perspectives. *Electrochem. Energy Rev.* **2019**, *2*, 1−28.
(7) Tabelin, C. B.; Dallas, J.; Casanova, S.; Pelech, T.; Bournival, G.; Saydam, S.; Canbulat, I. Towards a Low-Carbon Society: A Review of Lithium Resource Availability, Challenges and Innovations in Mining, Extraction and Recycling, and Future Perspectives. *Min. Eng.* **2021**, *163*, 106743.
(8) Vikström, H.; Davidsson, S.; Höök, M. Lithium Availability and Future Production Outlooks. *Appl. Energy* **2013**, *110*, 252−266.
(9) Tapia-Ruiz, N.; Armstrong, A. R.; Alptekin, H.; Amores, M. A.; Au, H.; Barker, J.; Boston, R.; Brant, W. R.; Brittain, J. M.; Chen, Y.; et al. 2021 Roadmap for Sodium-Ion Batteries. *J. Phys.: Energy* **2021**, *3*, 031503.
(10) Abraham, K. M. How Comparable Are Sodium-Ion Batteries to Lithium-Ion Counterparts? *ACS Energy Lett.* **2020**, *5*, 3544−3547.
(11) Nayak, P. K.; Yang, L.; Brehm, W.; Adelhelm, P. From Lithium-Ion to Sodium-Ion Batteries: Advantages, Challenges, and Surprises. *Angew. Chem. Int. Ed.* **2018**, *57*, 102−120.
(12) Sawicki, M.; Shaw, L. L. Advances and Challenges of Sodium Ion Batteries as Post Lithium Ion Batteries. *RSC Adv.* **2015**, *5*, 53129−53154.
(13) Hwang, J.-Y.; Myung, S.-T.; Sun, Y.-K. Sodium-Ion Batteries: Present and Future. *Chem. Soc. Rev.* **2017**, *46*, 3529−3614.
(14) Vineeth, S. K.; Tebyetekerwa, M.; Liu, H.; Soni, C. B.; Sungjemmenla; Zhao, X. S.; Kumar, V. Progress in the Development of Solid-State Electrolytes for Reversible Room-Temperature Sodium-Sulfur Batteries. *Mater. Adv.* **2022**, *3*, 6415−6440.
(15) Vasudevan, S.; Dwivedi, S.; Balaya, P. Overview and Perspectives of Solid Electrolytes for Sodium Batteries. *Int. J. Appl. Ceram. Technol.* **2023**, *20*, 563−584.
(16) Liu, Q.; Zhao, X.; Yang, Q.; Hou, L.; Mu, D.; Tan, G.; Li, L.; Chen, R.; Wu, F. The Progress in the Electrolytes for Solid State Sodium-Ion Battery. *Adv. Mater. Technol.* **2023**, *8*, 2200822.
(17) Yang, H.-L.; Zhang, B.-W.; Konstantinov, K.; Wang, Y.-X.; Liu, H.-K.; Dou, S.-X. Progress and Challenges for All-Solid-State Sodium Batteries. *Adv. Energy Sustainability* **2021**, *2*, 2000057.
(18) Sun, Y.-K. Promising All-Solid-State Batteries for Future Electric Vehicles. *ACS Energy Lett.* **2020**, *5*, 3221−3223.
(19) Yung-Fang, Y. Y.; Kummer, J. T. Ion Exchange Properties of and Rates of Ionic Diffusion in Beta-Alumina. *J. Inorg. Nucl. Chem.* **1967**, *29*, 2453−2475.
(20) Di Vona, M. L.; Traversa, E.; Licoccia, S. Nonhydrolytic Synthesis of NASICON of Composition $Na_3Zr_2Si_2PO_{12}$- A Spectroscopic Study. *Chem. Mater.* **2001**, *13*, 141−144.
(21) Kaus, M.; Guin, M.; Yavuz, M.; Knapp, M.; Tietz, F.; Guillon, O.; Ehrenberg, H.; Indris, S. Fast Na^+ Ion Conduction in NASICON-Type $Na_{3.4}Sc_2(SiO_4)_{0.4}(PO_4)_{2.6}$ Observed by ^{23}Na NMR Relaxometry. *J. Phys. Chem. C* **2017**, *121*, 1449−1454.
(22) Khireddine, H.; Fabry, P.; Caneiro, A.; Bochu, B. Optimization of NASICON Composition for Na^+ Recognition. *Sens. Actuators, B* **1997**, *40*, 223−230.
(23) Schlem, R.; Till, P.; Weiss, M.; Krauskopf, T.; Culver, S. P.; Zeier, W. G. Ionic Conductivity of the NASICON Related Thiophosphate $Na_{1+x}Ti_{2-x}Ga_x(PS_4)_3$. *Chem.—Eur. J.* **2019**, *25*, 4143−4148.
(24) Deng, Z.; Mishra, T. P.; Mahayoni, E.; Ma, Q.; Tieu, A. J. K.; Guillon, O.; Chotard, J. N.; Seznec, V.; Cheetham, A. K.; Masquelier, C.; Gautam, G. S.; Canepa, P. Fundamental investigations on the sodium-ion transport properties of mixed polyanion solid-state battery electrolytes. *Nat. Commun.* **2022**, *13*, 4470.
(25) Ma, Q.; Tsai, C. L.; Wei, X. K.; Heggen, M.; Tietz, F.; Irvine, J. T. Room temperature demonstration of a sodium superionic conductor with grain conductivity in excess of 0.01 S cm^{-1} and its primary applications in symmetric battery cells. *J. Mater. Chem. A* **2019**, *7*, 7766−7776.
(26) Chen, S.; Wu, C.; Shen, L.; Zhu, C.; Huang, Y.; Xi, K.; Maier, J.; Yu, Y. Challenges and Perspectives for NASICON-Type Electrode Materials for Advanced Sodium-Ion Batteries. *Adv. Mater.* **2017**, *29*, 1700431.
(27) Zhang, Z.; Ramos, E.; Lalère, F.; Assoud, A.; Kaup, K.; Hartman, P.; Nazar, L. F. $Na_{11}Sn_2PS_{12}$: A New Solid State Sodium Superionic Conductor. *Energy Environ. Sci.* **2018**, *11*, 87−93.
(28) Jansen, M.; Henseler, U. Synthesis, Structure Determination, and Ionic Conductivity of Sodium Tetrathiophosphate. *J. Solid State Chem.* **1992**, *99*, 110−119.
(29) Famprikis, T.; Dawson, J. A.; Fauth, F.; Clemens, O.; Suard, E.; Fleutot, B.; Courty, M.; Chotard, J. N.; Islam, M. S.; Masquelier, C. A New Superionic Plastic Polymorph of the Na^+ Conductor Na_3PS_4. *ACS Mater. Lett.* **2019**, *1*, 641−646.
(30) Hayashi, A.; Noi, K.; Sakuda, A.; Tatsumisago, M. Superionic Glass-Ceramic Electrolytes for Room-Temperature Rechargeable Sodium Batteries. *Nat. Commun.* **2012**, *3*, 856.
(31) Takeuchi, S.; Suzuki, K.; Hirayama, M.; Kanno, R. Sodium Superionic Conduction in Tetragonal Na_3PS_4. *J. Solid State Chem.* **2018**, *265*, 353−358.
(32) Krauskopf, T.; Culver, S. P.; Zeier, W. G. Local Tetragonal Structure of the Cubic Superionic Conductor Na_3PS_4. *Inorg. Chem.* **2018**, *57*, 4739−4744.
(33) Moon, C. K.; Lee, H. J.; Park, K. H.; Kwak, H.; Heo, J. W.; Choi, K.; Yang, H.; Kim, M. S.; Hong, S. T.; Lee, J. H.; Jung, Y. S. Vacancy-Driven Na^+ Superionic Conduction in New Ca-Doped Na_3PS_4 for All-Solid-State Na-Ion Batteries. *ACS Energy Lett.* **2018**, *3*, 2504−2512.
(34) Tanibata, N.; Noi, K.; Hayashi, A.; Tatsumisago, M. Preparation and Characterization of Highly Sodium Ion Conducting Na_3PS_4-Na_4SiS_4 Solid Electrolytes. *RSC Adv.* **2014**, *4*, 17120−17123.
(35) Chu, I. H.; Kompella, C. S.; Nguyen, H.; Zhu, Z.; Hy, S.; Deng, Z.; Meng, Y. S.; Ong, S. P. Room-Temperature All-solid-state Rechargeable Sodium-ion Batteries with a Cl-doped Na_3PS_4 Superionic Conductor. *Sci. Rep.* **2016**, *6*, 33733.
(36) Huang, B.; Zhang, J.; Shi, Y.; Lu, X.; Zhang, J.; Chen, B.; Zhou, J.; Cai, R. Low Ca^{2+} Concentration Doping Enhances the Mechanical Properties and Ionic Conductivity of Na_3PS_4 Superionic Conductors

https://doi.org/10.1021/acs.chemmater.3c02874
Chem. Mater. XXXX, XXX, XXX−XXX

Based on First-Principles. *Phys. Chem. Chem. Phys.* **2020**, *22*, 19816−19822.
(37) Kuhn, A.; Narayanan, S.; Spencer, L.; Goward, G.; Thangadurai, V.; Wilkening, M. Li self-diffusion in garnet-type $Li_7La_3Zr_2O_{12}$ as probed directly by diffusion-induced ^7Li spin-lattice relaxation NMR spectroscopy. *Phys. Rev. B* **2011**, *83*, 094302.
(38) Lunghammer, S.; Prutsch, D.; Breuer, S.; Rettenwander, D.; Hanzu, I.; Ma, Q.; Tietz, F.; Wilkening, H. M. R. Fast Na Ion Transport Triggered by Rapid Ion Exchange on Local Length Scales. *Sci. Rep.* **2018**, *8*, 11970.
(39) Luo, H.; Greene, R. G.; Ghandehari, K.; Li, T.; Ruoff, A. L. Structural Phase Transformations and the Equations of State of Calcium Chalcogenides at High Pressure. *Phys. Rev. B* **1994**, *50*, 16232−16237.
(40) Fritsch, C.; Hansen, A. L.; Indris, S.; Knapp, M.; Ehrenberg, H. Mechanochemical Synthesis of Amorphous and Crystalline $Na_2P_2S_6$-Elucidation of Local Structural Changes by X-Ray Total Scattering and NMR. *Dalton Trans.* **2020**, *49*, 1668−1673.
(41) Frydman, L.; Harwood, J. S. Isotropic Spectra of Half-Integer Quadrupolar Spins from Bidimensional Magic-Angle Spinning NMR. *J. Am. Chem. Soc.* **1995**, *117*, 5367−5368.
(42) Feng, X.; Chien, P. H.; Zhu, Z.; Chu, I. H.; Wang, P.; Immediato-Scuotto, M.; Arabzadeh, H.; Ong, S. P.; Hu, Y. Y. Studies of Functional Defects for Fast Na-Ion Conduction in $Na_{3-y}PS_{4-x}Cl_x$ with a Combined Experimental and Computational Approach. *Adv. Funct. Mater.* **2019**, *29*, 1807951.
(43) Duer, M. J. *Solid-State NMR Spectroscopy Principles and Applications*, 1st ed.; Blackwell Science Ltd Ed.ial Offices, 2002; p 567.
(44) Stanje, B.; Rettenwander, D.; Breuer, S.; Uitz, M.; Berendts, S.; Lerch, M.; Uecker, R.; Redhammer, G.; Hanzu, I.; Wilkening, M. Solid Electrolytes: Extremely Fast Charge Carriers in Garnet-Type $Li_6La_3ZrTaO_{12}$ Single Crystals. *Ann. Phys.* **2017**, *529*, 1700140.
(45) Epp, V.; Gün, Ö.; Deiseroth, H.-J.; Wilkening, M. Long-range Li^+ dynamics in the lithium argyrodite Li_7PSe_6 as probed by rotating-frame spin-lattice relaxation NMR. *Phys. Chem. Chem. Phys.* **2013**, *15*, 7123−7132.
(46) Wilkening, M.; Heitjans, P. From Micro to Macro- Access to Long-Range Li^+ Diffusion Parameters in Solids via Microscopic $^{6,7}Li$ Spin-Alignment Echo NMR Spectroscopy. *ChemPhysChem* **2012**, *13*, 53−65.
(47) Heitjans, P.; Kärger, J. *Diffusion in Condensed Matter*; Springer: Braunschweig, 1998; p 391.
(48) Kuhn, A.; Kunze, M.; Sreeraj, P.; Wiemhöfer, H. D.; Thangadurai, V.; Wilkening, M.; Heitjans, P. NMR Relaxometry as a Versatile Tool to Study Li Ion Dynamics in Potential Battery Materials. *Solid State Nucl. Magn. Reson.* **2012**, *42*, 2−8.
(49) Meyer, M.; Maass, P.; Bunde, A. Spin-lattice relaxation Non-Bloembergen-Purcell-Pound behavior by structural disorder and Coulomb interactions. *Phys. Rev. Lett.* **1993**, *71*, 573−576.
(50) Stainer, F.; Gadermaier, B.; Kügerl, A.; Ladenstein, L.; Hogrefe, K.; Wilkening, H. M. R. Fast Na^+ Ion Dynamics in the Nb^{5+} bearing NaSICON $Na_{3+x-z}Nb_zZr_{2-z}Si_{2+x}P_{1-x}O_{12}$ as probed by ^{23}Na NMR and Conductivity Spectroscopy. *Solid State Ionics* **2023**, *395*, 116209.
(51) Schweiger, L.; Hogrefe, K.; Gadermaier, B.; Rupp, J. L. M.; Wilkening, H. M. R.; Wilkening, H. Ionic Conductivity of Nanocrystalline and Amorphous Li10GeP2S12. The Detrimental Impact of Local Disorder on Ion Transport. *J. Am. Chem. Soc.* **2022**, *144*, 9597−9609.
(52) Hodge, I. M.; Ingram, M. D.; West, A. R. Impedance and Modulus Spectroscopy of Polycrystalline Solid Electrolytes. *J. Electroanal.* **1976**, *74*, 125−143.
(53) Jonscher, A. K. The "Universal" Dielectric Response. *Nature* **1977**, *267*, 673−679.
(54) Almond, D. P.; Duncan, G. K.; West, A. R. The Determination of Hopping Rates and Carrier Concentrations in Ionic Conductors by a New Analysis of AC Conductivity. *Solid State Ionics* **1983**, *8*, 159−164.
(55) Sidebottom, D. L. Dimensionality dependence of the conductivity dispersion in ionic materials. *Phys. Rev. Lett.* **1999**, *83*, 983−986.
(56) Irvine, J. T. S.; Sinclair, D. C.; West, A. R. Electroceramics: Characterization by Impedance Spectroscopy. *Adv. Mater.* **1990**, *2*, 132−138.
(57) Philipp, M.; Lunghammer, S.; Hanzu, I.; Wilkening, M. Partial Electronic Conductivity of Nanocrystalline Na_2O_2. *Mater. Res. Express* **2017**, *4*, 075508.
(58) Breuer, S.; Wilkening, M. Mismatch in cation size causes rapid anion dynamics in solid electrolytes: the role of the Arrhenius pre-factor. *Dalton Trans.* **2018**, *47*, 4105−4117.
(59) Mehrer, H. *Diffusion in Solids—Fundamentals, Methods, Materials, Diffusion-Controlled Processes*; Springer: Berlin: Heidelberg, 2007.
(60) Einstein, A. Über die von der molekularkinetischen Theorie der Wärme geforderte Bewegung von der ruhenden Flüssigkeiten suspendierter Teilchen. *Ann. Phys.* **1905**, *322* (8), 549−560.
(61) van Smoluchowski, M. Zur kinetischen Theorie der Brownschen Molekularbewegung und der Suspensionen. *Ann. Phys.* **1906**, *326*, 756−780.
(62) Gadermaier, B.; Stanje, B.; Wilkening, A.; Hanzu, I.; Heitjans, P.; Wilkening, H. M. R. Glass in Two Forms- Heterogeneous Electrical Relaxation in Nanoglassy Petalite. *J. Phys. Chem. C* **2019**, *123*, 10153−10162.
(63) Francisco, B. E.; Stoldt, C. R.; M'Peko, J. C. Lithium-ion trapping from local structural distortions in sodium super ionic conductor (NASICON) electrolytes. *Chem. Mater.* **2014**, *26*, 4741−4749.
(64) Meyer, W.; Neldel, H. Concerning the relationship between the energy constant epsilon and the quantum constant alpha in the conduction-temperature formula in oxydising semi-conductors. *Phys. Z.* **1937**, *38*, 1014−1019.
(65) Roeder, S.; Fukushima, E. *Experimental Pulse NMR: A Nuts and Bolts Approach*; Addison-Wesley Pub. Co., 1981; Vol. *198*, p 207.

https://doi.org/10.1021/acs.chemmater.3c02874
Chem. Mater. XXXX, XXX, XXX−XXX